

Optimal transport for mapping senescent cells in spatial transcriptomics

Nam D. Nguyen¹, Lorena Rosas², Timur Khaliullin², Peiran Jiang¹, Euxhen Hasanaj¹, Jose A. Ovando², Marta Bueno³, Melanie Konigshoff³, Oliver Eickelberg³, Mauricio Rojas², Ana L. Mora², Jose Lugo-Martinez^{1*}, and Ziv Bar-Joseph^{1,4*}

¹Computational Biology Department, School of Computer Science, Carnegie Mellon University, Pittsburgh, PA 15213, USA,

²Dorothy M. Davis Heart and Lung Research Institute, Division of Pulmonary, Critical Care and Sleep Medicine, Department of Internal Medicine, the Ohio State University, Columbus, OH, USA.

³Aging Institute, University of Pittsburgh School of Medicine/UPMC and Division of Pulmonary, Allergy and Critical Care Medicine, Department of Medicine, University of Pittsburgh, Pittsburgh, PA, USA.

⁴Machine Learning Department, School of Computer Science, Carnegie Mellon University, Pittsburgh, PA 15213, USA

*To whom correspondence should be addressed: jlugomar@andrew.cmu.edu; zivbj@andrew.cmu.edu

Abstract

Spatial transcriptomics (ST) provides a unique opportunity to study cellular organization and cell-cell interactions at the molecular level. However, due to the low resolution of the sequencing data additional information is required to utilize this technology, especially for cases where only a few cells are present for important cell types. To enable the use of ST to study senescence we developed scDOT, which combines ST and single cell RNA-Sequencing (scRNA-Seq) to improve the ability to reconstruct single cell resolved spatial maps. scDOT integrates optimal transport and expression deconvolution to learn non-linear couplings between cells and spots and to infer cell placements. Application of scDOT to existing and new lung ST data improves on prior methods and allows the identification of the spatial organization of senescent

24 cells, the identification of their neighboring cells and the identification of novel genes involved in
25 cell-cell interactions that may be driving senescence.

26 **1 Introduction**

27 Recent advancements in genomics technologies have facilitated the profiling of gene expression at
28 the single-cell level, unveiling valuable insights regarding the molecular heterogeneity of complex
29 biological systems. While single-cell RNA sequencing (scRNA-seq) has significantly enhanced
30 our comprehension of cell-type diversity, it lacks spatial information due to the dissociation of
31 cells. Spatial transcriptomics (ST) techniques enable the preservation of spatial information
32 within tissue samples but typically offer lower resolution or coverage compared to scRNA-seq
33 data. Hence, the integration of scRNA-seq and ST data becomes imperative for acquiring a
34 spatially informed single-cell resolution dataset [28]. This integration approach not only ensures
35 a more comprehensive understanding of the molecular heterogeneity within complex biological
36 systems but also retains the spatial context of gene expression.

37 Existing methods for integrating single-cell and spatial transcriptomics data primarily focus
38 on cell-type deconvolution. These methods decompose gene expression in a spatial spot into
39 linear combinations of fractions attributed to different cell types, utilizing the single-cell data
40 solely as a reference [24, 12, 30, 21, 5, 29, 2, 10]. While successful, these methods often struggle
41 when it comes to cell types with only a few cells [6, 32, 51]. Moreover, in cases where these
42 smaller cell types are very similar to cell types with larger number of cells, the assignment of
43 deconvolution methods often completely ignore these smaller cell types as shown in Results.

44 Cellular senescence, a state of permanent growth arrest, is implicated in various age-related
45 diseases. Understanding cellular senescence requires analyzing cell-cell communications at the
46 individual cell level, as the process exhibits heterogeneity, where only a few cells within a given
47 cell type enter a senescent state simultaneously. Additionally, paracrine senescence, in which a
48 senescent cell can induce senescence in neighboring cells, is of significant importance. Effective
49 communication between senescent cells and neighboring cells is crucial for the progression and
50 maintenance of the senescent phenotype [38, 13]. Senescent cells actively engage in intercellular
51 communication, primarily through the secretion of senescence-associated secretory phenotype
52 (SASP) factors, influencing neighboring and distant cells [13, 15]. However, the mechanisms
53 underlying these communications remain poorly understood. To address this gap, and to en-
54 able the study of cell-cell interactions for these small number of senescent cells within a cell
55 type using spatial transcriptomics, we propose an innovative computational framework that in-

56 tegrates single-cell and spatial transcriptomics data. This approach allows us to infer cell-cell
57 communications based on the proximity of cells, whether short- or long-range, shedding light
58 on the intricacies of senescence-associated intercellular signaling. This method offers a superior
59 alternative to organoids, where only cell types interact in an artificial environment.

60 Mapping individual cells to their spatial origins requires fine-grained mapping, which is prone
61 to imprecise results due to the similarity within cell types and the non-linear relationship between
62 gene expression levels in scRNA-seq and spatial transcriptomics [46]. Methods proposed for this
63 task compute a similarity score in a shared latent space. This similarity score is then coupled
64 with a statistical test to determine the significance of the assignment [46, 19]. Other techniques,
65 e.g., canonical correlation analysis or non-negative matrix factorization, for constructing shared
66 latent space have also been used [4, 43, 49]. In contrast, here, we utilize optimal transport
67 [40, 45], a mathematical framework that allows for the comparison and matching of probability
68 distributions. Specifically, we use optimal transport to learn the non-linear coupling between
69 cells and spots by aligning the distributions of gene expression profiles across these two datasets.
70 Our approach employs a probabilistic mapping, where the precision of the mapping is modulated
71 by incorporating the coarse-grained mapping of cell types obtained from the deconvolution task.
72 We solve these two complementary optimization tasks using a bilevel optimization approach [7],
73 based on the differentiable deep declarative network [16] (Figure 1).

74 Our approach incorporates two types of data, namely scRNA-seq and spatial transcriptomics,
75 as inputs. It employs iterative computations to perform cell type deconvolution and cell-to-spot
76 spatial mapping. As a result, it produces a coupling matrix between cells and spots that serves as
77 an initial integration outcome. This coupling matrix is subsequently used to infer the cell-to-cell
78 spatial neighborhood graph by aligning cells with spots possessing known spatial coordinates
79 (see Figure 1). Essentially, the spot coordinates play a crucial role in determining the physical
80 closeness between cells.

81 We tested scDOT on both, simulated and new spatial data. As we show, it can accurately
82 assign cells to their spot of origin outperforming prior methods for this task. For the new samples
83 for idiopathic pulmonary fibrosis (IPF), scDOT identifies the spatial distribution and cell-cell
84 interactions between senescence and non-senescence cells and the set of genes involved in these
85 interactions.

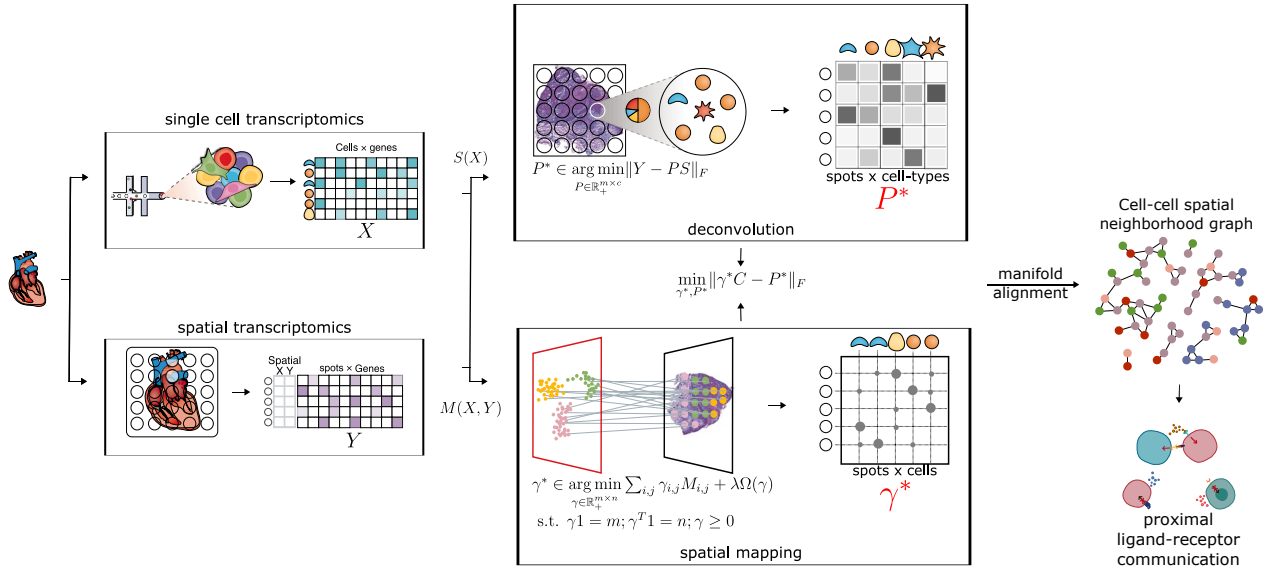


Figure 1: Method workflow: scDOT takes gene expression profiles from a scRNA-seq dataset and a spatial transcriptomics dataset as inputs. Additionally, cell type information for cells in the scRNA-seq data and spatial coordinates for spots in the spatial transcriptomics data are provided. scDOT simultaneously and in parallel learns the cell type fraction of each spot (deconvolution task) and the mapping between individual cells in the scRNA-seq data and individual spots in the spatial transcriptomics data (spatial reconstruction task). The resulting mapping matrix between cells and spots is then utilized to construct the cell-cell spatial neighborhood graph, where cells are connected if they are in close physical proximity.

86 2 Results

87 We developed an optimal transport (OT) method for mapping scRNA-Seq data to spatial tran-
 88 criptomics data. The method, illustrated in Figure 1 performs iterative computations for cell
 89 type deconvolution and cell-to-spot spatial mapping, resulting in the generation of the coupling
 90 matrix γ as an upstream integration outcome. This coupling matrix is then utilized to infer the
 91 cell-to-cell spatial neighborhood graph by aligning cells to spots with known spatial coordinates.

92 2.1 scDOT efficiently reconstructs individual cells to their spatial ori- 93 gins

94 We first tested scDOT on two simulation datasets where ground truth is known (Methods).
 95 The outcome of reconstructing single-cell data, i.e., the coupling matrix γ , when using simula-
 96 tion dataset 1 reveals that it successfully recovers the spatial origins of a high fraction of cells
 97 (56% to 76%, depending on a predefined threshold to determine high probability). γ represents
 98 probabilistic couplings and so a specific cell can be mapped to several location with different
 99 probabilities (which sum up to 1). We found that in most cases the distribution $\gamma_{:,j}$ exhibits is

100 extremely heavy-tailed and places a disproportionately high amount of probability densities at
101 0. We therefore defined a high probability of associating with a location based on distribution
102 properties (99th-, 95th-, 90th-quantile, or the 75th quantile (the third quantile) plus 1.5 times
103 the interquartile range (IQR) (Turkey’s fences)). Obviously, stricter the threshold, the fewer cells
104 that are correctly matched. However, even for a very high cutoff we find very large percentage
105 of correct matches (70% of cells at a threshold above the 90th quantile and 56% of cells at a
106 threshold above the 99th quantile when using synthetic data 1). However, the slower decay of
107 reconstruction results due to a more strict threshold is desirable and can be achieved through a
108 heavier tail in the distribution $\gamma_{:,j}$.

109 In addition, previous studies show that cell type deconvolution methods tend to miss rare cell
110 type [6]. In contrast when using OT we are able to map rare cell types to their spatial origins
111 (Fig 2b). In our simulation data, four types of cells can be classified as rare: 2-Mesothelium
112 and Submucosal Secretory have only 1 cell each, Myofibroblasts has 2, and Fibromyocytes has
113 7. The boxplots indicate that our approach successfully assigned all these rare cell types to their
114 correct spatial positions.

115 **2.2 Comparison to other methods on spatial mapping and cell type** 116 **deconvolution**

117 **Spatial mapping** We evaluate the performance of scDOT in spatial mapping and compare
118 it with other existing methods. Figure 2a presents the results for Synthetic data 1, where the
119 threshold is set above $Q3 + 1.5 \times IQR$. scDOT achieves the highest outcome at this threshold,
120 while the outcome of Novosparc is drastically decreased compared to the outcome at thresholds
121 above the 90th and 95th quantiles. This observation suggests that our probabilistic mapping
122 exhibits a heavier-tailed characteristic, which is a more desirable property for accurate spatial
123 mapping.

124 Furthermore, we find that the reconstruction results are influenced by the dataset used. For
125 Synthetic data 2, scDOT achieves a high outcome when the threshold is set above $Q3 + 1.5 \times IQR$,
126 with 76% of cells successfully reconstructed. However, stricter thresholds lead to a more rapid
127 decay in the outcomes, with only 50% of cells being reconstructed at the threshold above the
128 95th quantile. Nevertheless, across all cases, scDOT consistently outperforms both Novosparc
129 and the naive baseline of Random Sinkhorn.

130 In terms of accurately mapping rare cell types to their spatial positions, scDOT successfully
131 assigns all four rare cell types with a fraction of 1.0. However, Novosparc failed to accurately

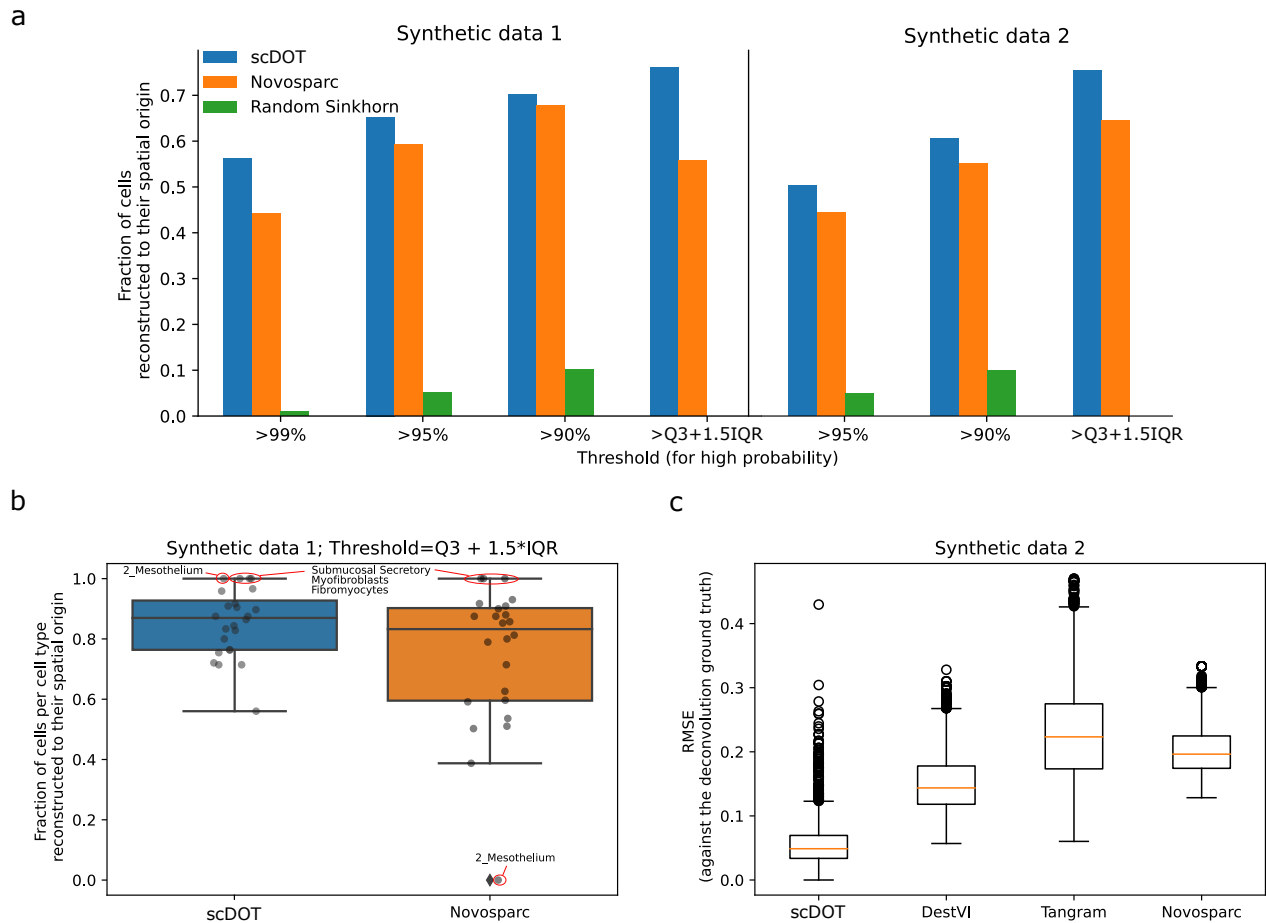


Figure 2: Performance on synthetic datasets. (a) OT results of simulation datasets 1 and 2 demonstrate that by using different thresholds to define a high probability, we can assign nearly 80% of cells to their spatial origin. scDOT was benchmarked against two other methods: Novosparc, a spatial reconstruction method based on Gromov-Wasserstein distance, and Random Sinkhorn, a naive method that learns the optimal transport coupling with a random cost matrix. The results demonstrate the superior performance of scDOT in all cases. (b) Detailed results of simulation data 1 (with a threshold higher than the 3rd quantile plus 1.5 times the IQR) highlight the effectiveness of scDOT and spatial mapping methods in general for rare cell types. The boxplots illustrate the fraction of correctly reconstructed cells per cell type. Each point represents a single cell type ($c = 24$). Among the considered rare cell types (2-Mesothelium and Submucosal Secretory with 1 cell, Myofibroblasts with 2 cells, and Fibromyocytes with 7 cells), scDOT successfully mapped these rare cell types to their exact spatial locations (fraction = 1.0), while Novosparc failed to map 2-Mesothelium to its spatial location (fraction = 0.0). (c) The root-mean-square-error (RMSE) of the deconvolved cell-type proportions compared to the ground truth is evaluated for synthetic data 2, consisting of 9 cell types across 3072 spots. scDOT, along with other methods including DestVI, Tangram, and Novosparc, is compared in terms of RMSE. The boxplots demonstrate that scDOT outperforms the other methods, as indicated by the lower RMSE values. The boxplots display the median (middle line), 25th and 75th percentiles (box), and 5th and 95th percentiles (whiskers).

132 map 2-Mesothelium to its spatial location, as indicated by a fraction of 0.0. Also, as indicated
133 in Figure 2a, scDOT mapped 76% cells correctly while Novosparc mapped 56% cells correctly;
134 these 20% differences is not shown in Figure 2b since the difference in the number of cells per
135 cell type is not considered.

136 **Deconvolution** To benchmark the results of cell type deconvolution, we applied scDOT to
137 synthetic data 2 and compared it with three other methods: DestVI [29], Tangram [3], and
138 Novosparc [37]. The synthetic dataset comprised nine cell types distributed across 3072 spots.
139 We specifically chose these three deconvolution methods as they represent distinct computational
140 techniques tailored for spatial transcriptomics data. DestVI is a probabilistic-based method,
141 Tangram utilizes deep learning, and Novosparc is an OT-based method. All three methods
142 require spatial transcriptomics data as input and scRNA-seq data as a reference. Comparing
143 the root-mean-square-error (RMSE) of the deconvolved cell type proportions with the ground
144 truth, scDOT outperformed the other three methods (see Figure 2c). The mean RMSE scores
145 for scDOT, DestVI, Tangram, and Novosparc were 0.06, 0.15, 0.23, and 0.20, respectively. It's
146 worth noting that Novosparc is not designed for direct computation of cell type deconvolution
147 but rather for mapping cells to spots. As a result, the deconvolution results are calculated by
148 multiplying the coupling matrix γ with the cell-by-cell type relation matrix C , i.e., $P = \gamma \times C$.

149 **2.3 Identifying the spatial patterns of the distribution of specific cell** 150 **types**

151 We used paired IPF scRNA-Seq and spatial dataset to test the ability of our mapping method to
152 infer cell-cell interactions (Figure 3). Among the 29 cell types (Methods), Multiciliated, Secre-
153 tory and Basal cells exhibited prominent and distinct spatial patterns. Notably, Multiciliated,
154 Secretory, and Basal cells were found to be in close proximity to each other, both in the upper
155 lobe and lower lobe of the tissue. This observation aligns with the traditional view of the airway
156 epithelial mucosal layer, which incorporates basal cells in close proximity to secretory and ciliated
157 cells, forming a tight unit. This unit serves as a physical barrier while remaining responsive to
158 the inhaled environment through interactions with submucosal fibroblasts, smooth muscle cells
159 and cells and molecules from the immune system [18].

160 Secretory and multiciliated cells are known to be located in close proximity to each other
161 within the respiratory tract, including the lungs. Together, they form a self-clearing mechanism
162 that efficiently removes inhaled particles from the upper airways, preventing their transfer to
163 deeper lung zones [9]. The coordinated action of multiciliated cells, with their motile cilia, and

164 secretory cells, responsible for mucus production and secretion, enables the effective clearance
165 of inhaled particles and maintains the integrity of the respiratory system [27].

166 Basal cells, positioned closer to the basement membrane, further contribute to the orga-
167 nization and functioning of the airway epithelium. They provide structural support and are
168 responsible for the regeneration and repair of the airway epithelial layer [18].

169 The spatial organization of Multiciliated, Secretory, and Basal cells in close proximity to
170 each other emphasizes their interdependence and coordinated functioning in maintaining the
171 respiratory barrier and facilitating efficient clearance mechanisms. This finding underscores the
172 significance of the spatial arrangement and interactions of diverse cell types within the airway
173 epithelium for the overall homeostasis and defense of the respiratory system.

174 Conversely, immune cell types such as Macrophages and T cells lineage, which were charac-
175 terized by a larger number of cells, displayed a more scattered distribution throughout the tissue.
176 Yet, the spatial distribution of these two cell types are complementary to some degree (Figure
177 3 and 4, Supplementary figures), reflecting the fact that they are both important components
178 of the immune system and play complementary roles in defending against infections and main-
179 taining immune homeostasis. On the other hand, cell types with a smaller cell count, such as
180 smooth muscle (consisting of only 2 cells in total), exhibited a spatial arrangement in adjacent
181 spots (Supplementary figures).

182 These patterns were also observed in the unpaired data, particularly with regards to the
183 multiciliated lineage and secretory cell types (Figure 3), demonstrating the generality of our
184 approach on unpaired datasets.

185 **2.4 Cell-cell proximity analysis**

186 To quantitatively illustrate the spatial distribution and proximity of multiciliated, secretory, and
187 basal cells described in section 3.3 of this paper, we employed the neighborhood enrichment score.
188 This score between two cell types represents the z-score derived from a permutation test that
189 tallies the neighboring spots consisting of either cell type. Consistent with the spatial patterns
190 depicted in section 3.3 and Figure 3, we observed the highest enrichment score between the
191 multiciliated lineage and itself across various datasets (69.46 in the upper lobe of familial IPF
192 paired data, 29.31 in the lower lobe of the same data, and 47.98 in the IPF unpaired data). The
193 score between Multiciliated and Secretory cell types is also one of the highest (19.40 in the upper
194 lobe of the paired dataset, 12.25 in the lower lobe, and 5.06 in the unpaired dataset). In contrast,
195 the scores between Macrophages and T cells are among the lowest across datasets, with scores

196 of -25, -5.75, and -15.83 in the upper lobe, lower lobe, and unpaired dataset, respectively. These
197 scores reflect the fact that they are complementary, as indicated in section 3.3 (see Supplementary
198 Figure 1). It is important to note that the neighborhood enrichment scores were estimated at
199 the spot-level and only considered the dominant cell type of each spot, which is defined as the
200 cell type with the highest proportion within that particular spot.

201 At the cell level, we constructed a cell-cell spatial proximity graph based on OT placement
202 (see Methods). The graph was then summarized by cell types, quantifying the physical prox-
203 imity between each cell type by counting the direct neighboring cells within the same type (see
204 Supplementary Figure 1d and e, Supplementary Table 1). Once again, the multiciliated lineage
205 exhibited the highest normalized counts with itself across datasets, consistent with the results
206 obtained from the enrichment score and described in Section 3.3. In the paired dataset, basal
207 and secretory cells also demonstrated a strong association with the airway epithelium, providing
208 additional evidence for the spatial organization of the respiratory system as discussed in Section
209 3.3. In contrast, immune cells such as T cells and macrophages displayed connections to various
210 cell types, reflecting their dispersed distribution throughout the tissue. Notably, in the IPF
211 lung sample, fibroblast cells exhibited a distinct spatial pattern and were found to be in close
212 proximity to α -smooth muscle cells and myofibroblast cells, supporting previous research sug-
213 gesting that α smooth muscle actin-expressing fibroblasts, referred to as myofibroblasts, serve as
214 markers of progressive lung injury and play a central role in detrimental remodeling and disease
215 progression [41, 20] (Supplementary Figure 1, Supplementary Table 1, Section 3.6).

216 2.5 Identification of senescent markers

217 For cellular senescence analysis, we profiled two new spatial datasets. The first included paired
218 scRNA-Seq data from a familial IPF lung sample, and the other consists of unpaired data from
219 an IPF lung sample (Methods).

220 **Paired data of familial IPF lung sample** We first identified in the scRNA-seq data,
221 cell types with a large fraction of cells exhibiting senescent. For this, we used a list of 68 senescent
222 marker genes (*Methods*). Within each cell type, we separated the cells into senescent and non-
223 senescent cells (Figure 4a, b). For this familial IPF lung sample, the ratio of senescent cells to
224 non-senescent cells is low. For most cell types we observed very few senescent cells. For other we
225 found more. For example, for Mast cells, T cell lineage, and Airway epithelium we identified 14%,
226 13%, and 17%, respectively. We thus focused on these three cell types. for these we had 24, 193,
227 and 3 senescent cells for Mast cells, T cell lineage, and Airway epithelium, respectively. Next,

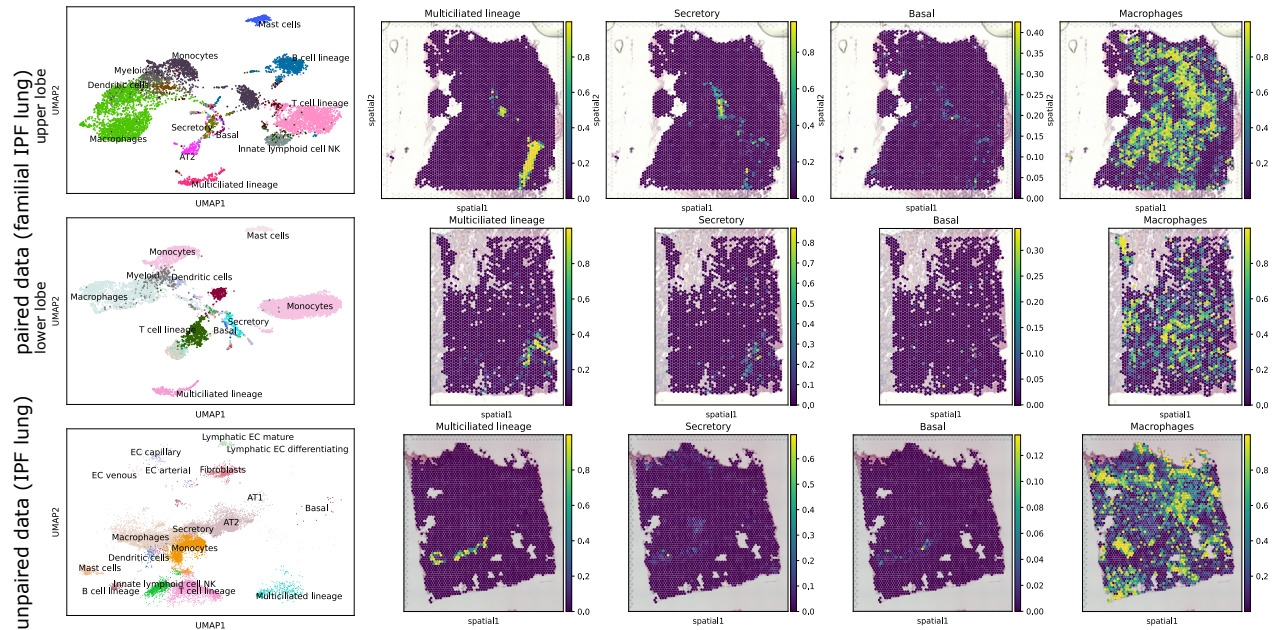


Figure 3: Spatial distribution patterns of multiciliated, secretory, basal, and macrophage cells across different datasets. **Top:** A UMAP representation of scRNA-seq data, along with the spatial patterns of the selected cell types in the upper lobe slice of the paired familial IPF lung. **Middle:** A UMAP representation of scRNA-seq data and the corresponding cell types in the lower lobe slice of the same sample. **Bottom:** A UMAP representation and spatial distribution of selected cell types in the unpaired IPF lung sample. Notably, multiciliated, secretory, and basal cell types exhibit distinct and prominent spatial patterns. Importantly, these cell types consistently exhibit close proximity to each other across all three datasets, consistent with previous studies on the organization of the respiratory system [18, 9, 27].

228 we manually annotated the regions where senescent cells from different cell types are collocated
229 (Figure 4b, c). For these regions we computed differentially expressed genes (DEG) w.r.t. the
230 rest of the tissue. As expected, given the way we selected these regions we found among the top
231 ranked DEG IGFBP4 and IGFBP7 (t-test p-values are $1.1e-11$ and $7.2e-07$ respectively), which
232 are both senescent marker genes (Figure 4d). We next performed gene set enrichment analysis
233 (GSEA) with this ranked gene list and a gene set of 340 senescent markers (which is a superset
234 of the 68 senescent marker genes set we used for re-annotation, Supplementary Data 1), we
235 confirmed that cellular senescence is enriched—with p-value = 0.006002; FDR = 0.006002, and
236 the normalized enrichment score is 1.726—in the annotated region (Figure 4d). The leading-edge
237 subset of genes in this analysis comprised IGFBP4, IGFBP7, FGF7, THBS1, IGF1, IGFBP6,
238 IL6, SERPINE2, PIM1, ALDH1A3, SERPINE1, COL1A2, ANGPTL4, CYP1B1, and PLAU.
239 While IGFBP4 and IGFBP7 belong to the initial set of 68 senescent marker genes, the remaining
240 genes are part of the larger set of 340 senescent marker genes. Of particular note, IGFBP4 and
241 IGFBP7 are SASP factors that have been identified as key components needed for triggering
242 senescence in young mesenchymal stem cells (MSC) [42]. The pro-senescent effects of IGFBP4
243 and IGFBP7 are reversed by single or simultaneous immunodepletion of either proteins from the
244 conditioned medium (CM) from senescent cells [42]. According to a previous study, prolonged
245 IGF1 treatment leads to the establishment of a premature senescence phenotype characterized
246 by a unique senescence network signature [34]. Combined IGF1/TXNIP-induced premature
247 senescence can be associated with a typical secretory inflammatory phenotype that is mediated
248 by STAT3/IL-1A signaling [34].

249 **2.6 Inferring Cell-Cell interactions driving senescence**

250 We also looked at the cell type neighborhood of senescent cells. These are summarized in Figure
251 5a. We observe that senescent cells are often close to non-senescent cells of the same type (e.g.,
252 senescent T cells to non-senescent T cells) which can explain why some cell types have a much
253 higher percentage of senescent cells than others.

254 Utilizing the CellPhoneDB [11], we further identified the ligand-receptor (LR) pairs involved
255 in the cell-cell interactions within the neighborhood of senescent cells (i.e., within the graph
256 G') (Figure 5d). We observed that 11 senescent markers, namely B2M, CALR, CCL5, CD44,
257 HMGB1, IGF1R, MIF, TNF, VIM, MMP9, and TNFRSF1B, were significantly overrepresented
258 in the list of ligands and receptors identified by CellPhoneDB (hypergeometric test p-value =
259 0.00072). Among the LR pairs involved in senescent-to-senescent cell-cell communication (i.e.,

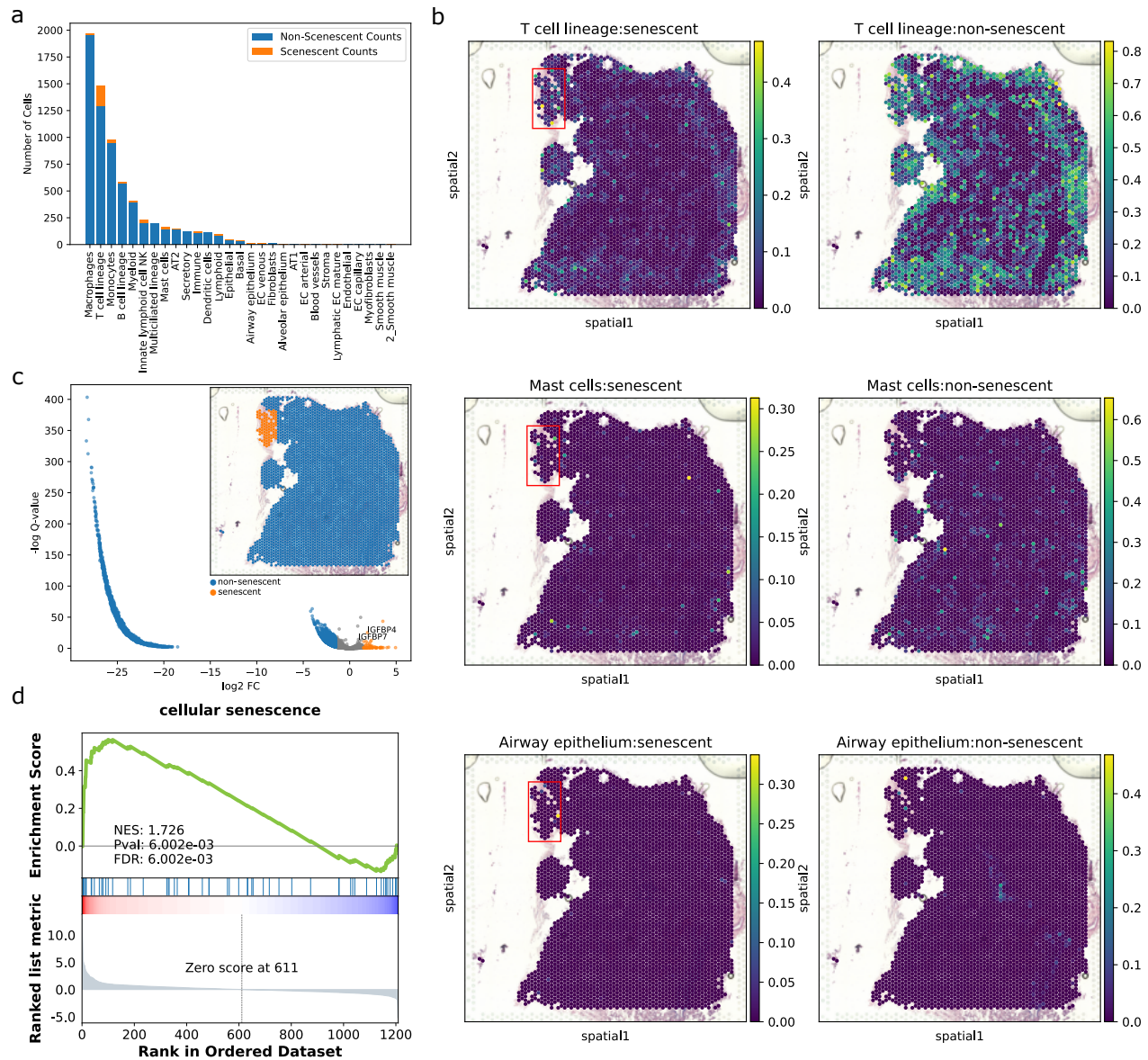


Figure 4: Analysis of cellular senescence reveals the spatial collocation of senescent cells. (a) The number of senescent cells and non-senescent cells for each cell type is depicted. T cell lineage, mast cells, and airway epithelium exhibit the highest fraction of senescent cells. (b) Spatial distribution of senescent and non-senescent cells for the three aforementioned cell types. Notably, the three different senescent cell types are spatially collocated in the upper left corner of the tissue. (c) Differentially expressed genes for the manually annotated senescent region (colored in orange) in the upper left corner of the tissue (as depicted in panel (b) of this figure and the upper right corner of this panel). Among the top-ranked DEGs are IGFBP4 and IGFBP7, which are also senescent marker genes. (d) Gene set enrichment analysis (GSEA) plot. The top-ranked DEGs (as shown in panel (c) of this figure) are enriched in the gene set consisting of 340 senescent marker genes.

260 between senescent T cells), most of the pairs include senescent marker genes. The other remaining
261 LR pairs involve the HLA gene family (which is essential for T cell activation). For example,
262 HLA-E acts as an inhibitory signal for NK and CD8 T cells—and depletion of HLA-E renders
263 senescent cells susceptible to elimination by both NK and CD8 T cells [39]. Another LR pair
264 involves S100A8, which increases with age, inducing inflammation and cellular senescence-like
265 phenotypes in oviduct epithelial cells [35, 14].

266 **Unpaired data from IPF lung sample** To demonstrate the general utility of the method
267 for unpaired data, we performed the same analysis as described for the paired data mentioned
268 above for another spatial dataset we profiled, this time without matched scRNA-Seq (Methods).
269 Using a scRNA-seq dataset of an IPF lung sample, we were still able to identify several of the
270 same senescence cell types as in the paired dataset, including T cells and mast cells. There were
271 300 assigned senescent cells out of the total 3747 T cells and 11 assigned senescent mast cells
272 out of the total 249 mast cells. We also observed high fraction of senescence cells for other cell
273 types including for fibroblasts (290 out of the total 461 fibroblast cells) and 2-smooth muscle (8
274 out of 21).

275 We again observed that senescence cells co-localized in the same regions (Figure 6a). While
276 T cells tended to be distributed throughout the tissue, there is a high fraction of senescent cells
277 co-localized with fibroblasts and mast cells (Figure 6a). Fibroblasts and 2-smooth muscle cells
278 co-localized in specific regions, with a total of four overlapping regions as depicted in Figure
279 6a. Since senescent cells tend to co-localize with other cells of the same type, most senescent
280 fibroblast cells and 2-smooth muscle cells also co-localized (except for the region in the upper
281 left corner of the tissue, which exhibited only senescent fibroblast cells). These observations of
282 senescent spatial distribution align with previous studies suggesting that senescent cells have
283 the potential to influence neighboring cells through processes collectively referred to as the
284 senescence-associated secretory phenotype [31].

285 Figure 6b and c illustrate the physical proximity among cells of different cell types. Similar
286 to the paired data of the familial IPF lung sample, senescent cells are closely clustered together
287 and near cells of the same type. As shown in Figure 6b, the senescent T cells are adjacent to
288 other T cells, mast cells, and macrophages. The cell-to-cell spatial neighborhood graph, with
289 nodes representing senescent T cells and their immediate neighbors, is depicted in Figure 6c. The
290 validity of this neighborhood graph is assessed in Supplementary Analysis. For a more specific
291 focus on senescent fibroblasts, a cell-to-cell neighborhood graph can be found in Supplementary
292 Figure 2.

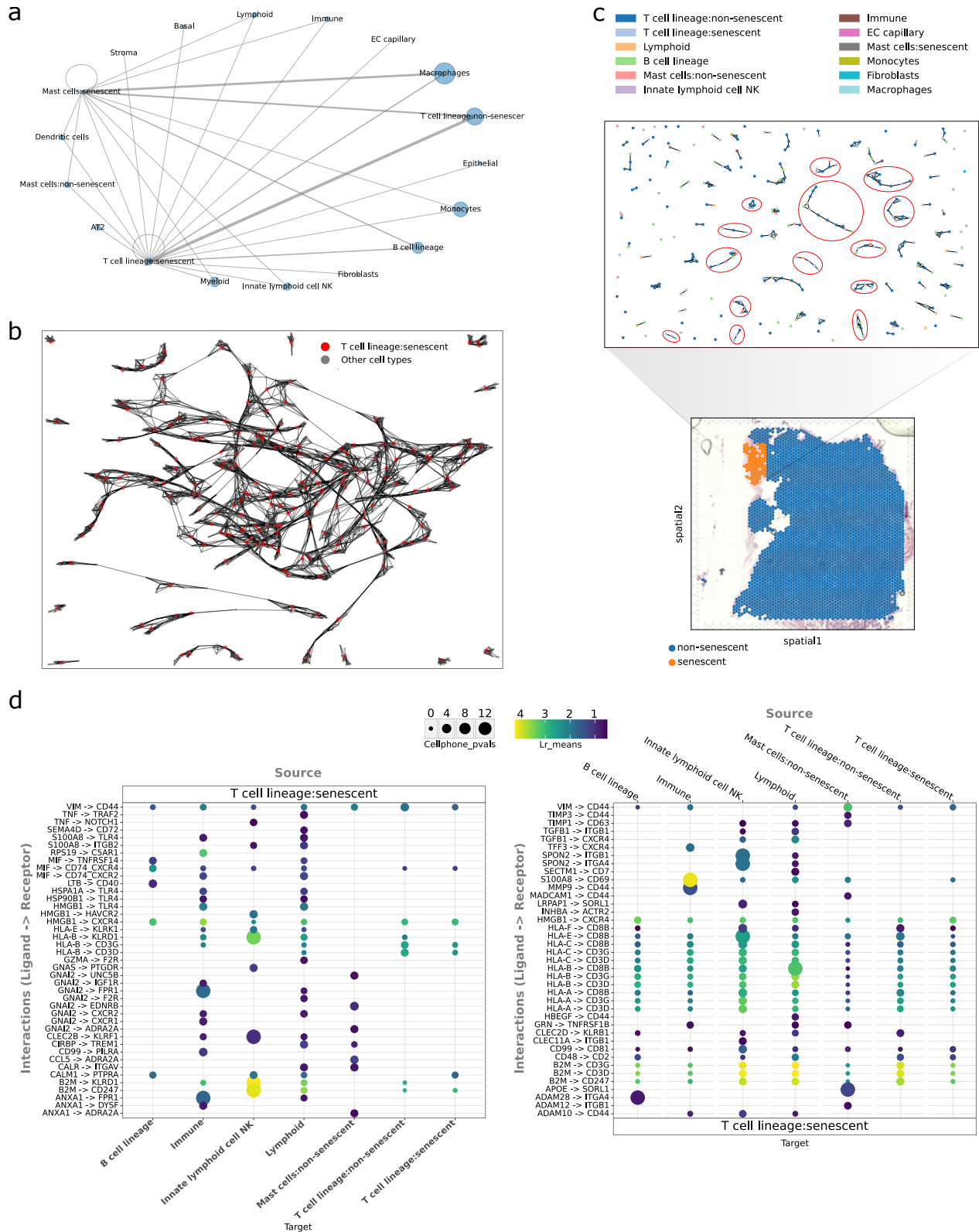


Figure 5: Analysis of senescent cell-cell communication in the upper lobe of the familial IPF lung sample. (a) The graph summarizes the spatial neighborhood of senescent mast cells and T cell lineage. Nodes represent cell types, and edges indicate direct neighboring relations in physical proximity. The size of each node corresponds to the number of cells within a cell type, while the width of the edges represent the number of neighboring cells of a specific cell type (i.e., the total node degree per neighboring cell type). Edges representing a small number of neighbors are omitted. As can be seen, senescent cells are close to both non-senescent cells within the same cell types and senescent cells belonging to different cell types. (b) Cell-cell spatial neighborhood of senescent cells for the T cell lineage. The validity of this neighborhood graph is assessed in Supplementary Analysis. (c) The subgraph of the cell-cell neighborhood depicted in panel (b), specifically showing the cells located in the senescent region (colored orange). (d) The results from CellphoneDB display the co-expressed ligand-receptor pairs between senescent cells of the T cell lineage and all other cells within the subgraph illustrated in panel (c).

293 3 Discussion

294 In this study, we introduced a novel method for integrating single-cell and spatial transcrip-
295 tomics, addressing the simultaneous tasks of cell type deconvolution and spatial reconstruction.
296 The challenge of spatial reconstruction lies in the non-linear relationship between gene expression
297 profiles of single-cells and the spatial transcriptomics data [46], as well as the inherent uncer-
298 tainty in high-resolution mapping. However, by incorporating internal references from cell type
299 deconvolution, we can modulate and enhance the precision of this task.

300 Our method, scDOT was shown to efficiently and accurately assign individual cells to their
301 spatial origins using synthetic data. By combining OT and deconvolution scDOT improves
302 on all prior methods we compared to. We also used scDOT to study and analyze new paired
303 and unpaired spatial transcriptomics data from IPF and familial IPF lungs. We observed that
304 senescent cells tend to co-localize in specific regions and are in close proximity to cells of the
305 same type. While the distribution of senescent T cells appears sparse in both datasets, we
306 noted a denser population of senescent fibroblast cells in the IPF lung compared to the familial
307 IPF lung, which can be explained by the paracrine senescence and is consistent with previous
308 studies indicating that senescent fibroblasts contribute to the pathogenesis of IPF through various
309 mechanisms [1, 48, 26].

310 The integration of single-cell and spatial transcriptomics has been a topic of interest in recent
311 years [28], with a number of multiview learning approaches suggested [36]. A crucial aspect of
312 this integration is assessing the similarity of gene expression levels between cells and spatial
313 spots. Unlike prior methods that utilized optimal transport, which rely on fixed cost matrices to
314 represent the dissimilarity between cells and spots, scDOT utilizes a differentiable optimization
315 layer in a deep declarative network to dynamically learn the cost matrix [16]. This use of optimal

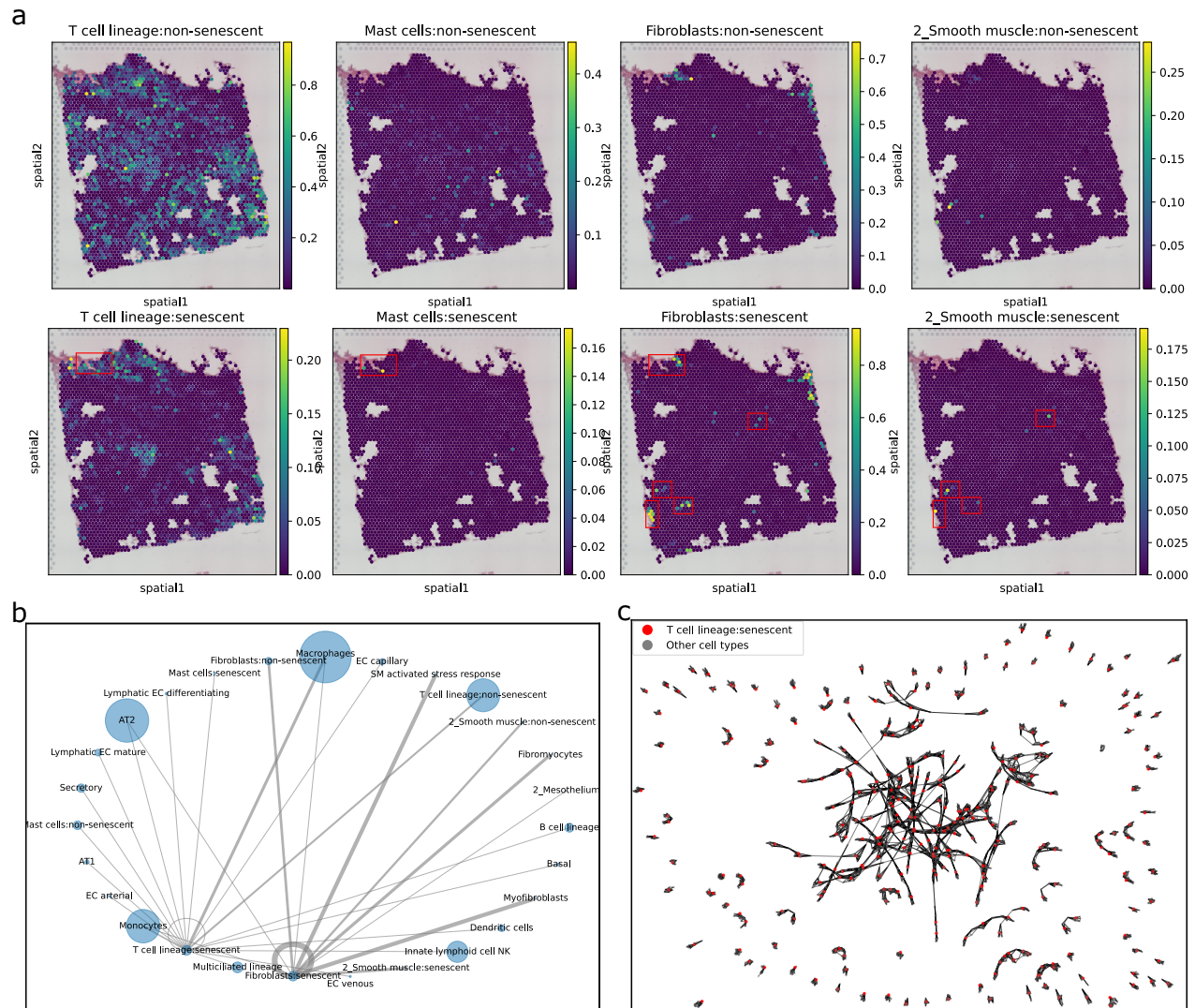


Figure 6: The analysis of senescent cell-cell neighborhood for unpaired IPF dataset. (a) Spatial distribution of senescent and non-senescent cells for T cells, Mast cells, Fibroblasts, and 2-Smooth muscle. Red rectangles indicate regions where senescent cells of multiple types are co-located. (b) The graph summarizes the spatial neighborhood of senescent Fibroblasts and T cells. Nodes represent cell types, and edges represent direct neighboring relations in physical proximity. The size of the nodes corresponds to the number of cells within a cell type, and the width of the edges corresponds to the number of neighboring cells of a specific cell type (i.e., the total node degree per neighboring cell type). Edges representing a small number of neighbors are omitted. The graph demonstrates that senescent cells are neighbors to non-senescent cells within the same cell types, as well as to senescent cells belonging to different cell types. (c) The cell-cell spatial neighborhood graph of senescent cells of the T cell lineage. The validity of this neighborhood graph is assessed in Supplementary Analysis.

316 transport can be formulated as a domain adaptation problem, and the learned cost matrix holds
317 potential for further applications involving mass transportation between the two modalities of
318 other types of data.

319 Comparative studies and benchmarks exist for cell type deconvolution in spatial transcrip-
320 tomics data [23, 24, 50]. Since there is no universal evaluation metric that applies to all scenarios,
321 comparisons among methods depend on datasets and evaluation metrics used, such as root mean
322 square error and Lin’s concordance correlation coefficient, which may not consistently correlate
323 [23, 6]. In our paper, we compared our method with recent approaches representing compu-
324 tational techniques like deep learning, probabilistic modeling, and optimal transport. While
325 the performance of these methods may vary, certain high-performance methods, particularly
326 Tangram [3], have been reported [23, 24, 50]. Additionally, note the normalization of our syn-
327 thetic data 2, making methods utilizing count matrices as input, such as Stereoscope [2] and
328 Cell2Location [21], inapplicable.

329 An important component of our biological analysis focused on IPF and familial IPF lung
330 tissue was the identification of senescent cells. Evaluating cellular senescence poses challenges
331 as there are various approaches, such as assessing senescent gene markers or morphological
332 features of senescent cells. Additionally, different cell types or diseases may require distinct
333 sets of senescent markers due to the complex nature of the senescence process. In our study, we
334 employed a combined list of senescent markers and categorized cells within each cell type as either
335 senescent or non-senescent. However, senescent states can exist on a continuum, ranging from
336 non-senescence to primary senescence, and different markers may be associated with primary and
337 secondary senescence. Still, using scDOT we were able to identify cell-cell spatial neighborhood,
338 which can aid in assessing senescent cells in close physical proximity. It also allowed us to explore
339 how senescent cells reorganize and impact their environment and nearby cells. Cells neighboring
340 senescent cells can transition into a secondary senescent state. Hence, the influence of senescence
341 can be approached as a diffusion problem within a network, where cells reach a senescent state
342 through contact with senescent neighbors. This network-based diffusion approach, relying on the
343 spatial mapping of individual cells to their origins, holds promise for fruitful future investigations.

344 scDOT is implemented in PyTorch and is available for download from
345 <https://github.com/namtk/scDOT>.

4 Methods

4.1 Data sets

To investigate the effects of the proposed method that combines cell-type deconvolution and spatial reconstruction, we collected both synthetic and real data. Since there is no immediate method to assess the performance of cell-type deconvolution and spatial reconstruction tasks on real data, we generated two simulation datasets to evaluate and benchmark scDOT as well as other related methods against the ground truth. It is important to note that, for benchmarking the deconvolution task, methods designed for spatial reconstruction can be utilized. However, for benchmarking the reconstruction task, methods solely designed for cell-type deconvolution cannot be used, as inferring the fine-grained mapping γ of individual cells from a coarse-grained mapping P of cell clusters poses a challenging inverse problem, even though inferring the cell type proportion P from the coupling matrix γ is straightforward ($P = \gamma \times C$).

4.1.1 Synthetic data sets

Synthetic data set 1 The synthetic data 1 is generated based on Gaussian Process (GP) by assuming that the nearby spots have similar proportions of cell types as well as gene expressions [29]. Here, we used scRNA-seq data of an IPF lung tissue and projected the cells from this data onto grids, which represent the spatial coordinates obtained from a different IPF lung sample's upper lobe lung slice. Thus, scRNA-seq data is real while spatial locations are synthetic for this dataset. See Supporting methods for more details.

Synthetic data set 2 For the synthetic data 2, we conducted simulations using gene expression data from individual cells obtained through multiplex error-robust fluorescence in situ hybridization (MERFISH) in the mouse medial preoptic area (MPOA) [32, 33]. By aggregating the gene expression information of cells within spatially contiguous pixels, we created a representation of the spatial organization. See Supporting Methods for more details.

4.1.2 Real data sets

Preparation and data collection of single-cell RNA sequencing and spatial transcriptomics Tissue samples were obtained by the Human Tissue Biorepository at The Ohio State University from the explanted lungs of patients diagnosed with idiopathic pulmonary fibrosis (IPF) and familial IPF after a Total Transplant Care Protocol informed consent and

375 research authorization from the patient. The tissue biorepository operates in accordance with
376 NCI and ISBER Best Practices for Repositories.

377 *For single-cell RNA sequencing (scRNA-seq):* Samples of 15 g of upper and lower lobe lung
378 parenchyma tissue were washed with PBS, minced finely with scalpels, and digested using an
379 enzyme cocktail (1 mg/mL of liberase DL, DNase I, DMEM) for 2 hours at 37°C with rocking.
380 Cell suspension was filtered through a serial filter of 300 μm , 100 μm , and 70 μm strainers.
381 After straining, the cell suspension was centrifuged at 500g for 7 minutes, the supernatant was
382 removed, and 1x RBC lysis buffer was added to the pellet and incubated at 4°C for 7 minutes
383 and then filtered through a 40 μm strainer to remove the agglomerated dead cells. Finally,
384 cell number and viability were determined using a countess automatic cell counter (Invitrogen).
385 Whole lung cell suspension was loaded on the Chromium Controller, according to 10x Genomics
386 protocol. 3' Gene Expression libraries were sequenced on Illumina sequencer with read lengths
387 of 28 cycles Read 1, 10 cycles i7 index, 10 cycles i5 index, 90 cycles Read 2. ScRNA-seq data
388 was extracted from the raw sequencing data using Cell Ranger (version 7.1.0, 10x Genomics).

389 *For spatial transcriptomics:* Tissue sections of $\leq 6.5 \times 6.5$ mm from the upper and lower lobe
390 of lung parenchyma were used for spatial analysis. After collection, samples were fixed for 24
391 hours in 10% neutral buffered formalin and embedded in paraffin (wax) to create a formalin-fixed
392 paraffin-embedded (FFPE) block. Sections of 5 μm were then cut from the FFPE blocks onto
393 Visium slides (10x Genomics) and processed according to the manufacturer's protocol. Scan
394 of H&E staining was performed with EVOSTM M7000 microscope (Invitrogen) using a 10x
395 objective. FFPE libraries were prepared according to 10x Genomics protocol and sequenced on
396 Illumina sequencer to a read depth of at least 25k reads/spot, with read lengths of 28 cycles
397 Read 1, 10 cycles i7 index, 10 cycles i5 index, 50 cycles Read 2. Spatial transcriptomics data
398 was extracted from the raw sequencing data using Space Ranger (version 2.0.0, 10x Genomics).

399 **Paired familial IPF lung data set** We obtained two paired datasets of single-cell and
400 spatial transcriptomics from a patient with familial IPF lung, one of which is from the upper
401 lobe slice and the other from the lower lobe slice. The upper lobe pair contains 6762 cells and
402 3336 spots while the lower lobe pair contains 6173 cells and 2246 spots. For each of these two
403 paired datasets, we preprocessed the data by (1) removing lowly expressed genes of both two
404 data modalities, keeping genes that have at least 10 counts, and (2) removing cells with low
405 counts, keeping cells that have at least 500 counts and 500 genes expressed, then (3) obtaining
406 the common gene sets for both modalities by taking the intersection of the two gene sets.

407 The cell type annotations were transferred from the Lung cell atlas (HLCA) using scArches

408 and FastGenomics platform.

409 To re-annotate cells that reflect senescent states, we utilized a list of 68 senescent markers
410 (Supplementary Data 1), then calculated the average expression of the marker genes across all
411 cells. Next, senescent cells were identified as having a higher than 95 percentile of average
412 expression of the marker genes.

413 **Unpaired IPF lung data set** To demonstrate the general utility of the method even for
414 non-paired data, we obtained an unpaired scRNA-seq and spatial transcriptomics dataset from
415 two different IPF patients. While the preparation for spatial transcriptomics is the same as for
416 the paired data, the preparation for single-cell RNA sequencing is described as follows. Single-cell
417 sequencing of human lung tissue was performed as previously described [44, 17]. In short, human
418 lung tissue (IPF) was homogenized, and 4 g of tissue were digested by dispase/collagenase (Col-
419 lagenase: 0.1U/mL, Dispase: 0.8U/mL, Roche) for 1 hour at 37°C. Samples were successively
420 filtered through nylon filters (100 μm and 20 μm) followed by a percoll gradient. Single ep-
421 ithelial cell suspensions were loaded onto a Chromium single-cell chip (Chromium™ Single Cell 3'
422 Reagent Kit, v2 Chemistry) to obtain single-cell 3' libraries for sequencing. cDNA obtained after
423 droplet reverse transcription was amplified for 14 cycles and analyzed using Agilent Bioanalyzer.
424 The barcoded libraries were sequenced using Illumina NextSeq-500 through the University of
425 Pittsburgh Genomics Core Sequencing Facility, aiming for 100,000 reads per cell and capturing
426 10,000 per library.

427 The single-cell data contains 25,260 cells, and the spatial data, which consists of an upper
428 lobe lung slide, contains 3,412 spots. The preprocessing, cell type annotation, and senescence
429 re-annotation were carried out following the same procedures as for the paired familial IPF lung
430 dataset.

431 It is important to note that, since the familial IPF lung datasets are paired, the coordinates
432 of cells after spatial reconstruction represent the actual tissue coordinates. However, for the
433 unpaired IPF lung dataset, the inferred cell coordinates do not directly reflect the actual tissue
434 coordinates. Instead, they serve as an intermediate step to infer the relative spatial relationships
435 among cells.

436 4.2 Cell type deconvolution

For gene expression, cell type deconvolution can be formulated as a nonnegative least squares (NNLS) problem, where the goal is to estimate the relative abundances of different cell types by solving for the nonnegative coefficients of a linear combination of their respective gene expression

profiles. Specifically, a multicellular resolution spatial transcriptomics profile $Y \in \mathbb{R}^{m \times p}$ of p genes across m spots each of which contains transcripts from multiple cells can be represented as $Y = PS$ in which $P \in \mathbb{R}^{m \times c}$ is the cell type proportions to be estimated and $S \in \mathbb{R}^{c \times p}$ is the signature matrix consisting of known gene expression profiles for each cell type of the total c cell types. We solved for P the following nonnegative least squares problem:

$$P^* \in \arg \min_{P \geq 0} \|Y - PS\|_F \quad (1)$$

437 There are several solvers available for solving a NNLS problem, including Lawson-Hanson's
 438 active set method [22]. Here, we used projected gradient descent [25].

439 4.3 Mapping single cell to spatial images

The spatial reconstruction task involves assigning cells from scRNA-seq data to a predicted corresponding location in a tissue sample. Note that such assignment, implicitly, also provides deconvolution of the spot data assuming that the cell types for cells in the scRNA-Seq data are known. Here we formulate this as an optimal transport (OT) problem from scRNA-seq dataset $X \in \mathbb{R}^{n \times p}$ of p genes across n cells to spatial transcriptomics dataset $Y \in \mathbb{R}^{m \times p}$ of p genes across m . OT is commonly used to model the coupling between two probability distribution. In our case we use it to model the transport of gene expression from one dataset to another in an optimal way. By solving the optimal transport problem, it is possible to estimate the optimal coupling and quantify the degree of similarity between the datasets. Formulating the spatial reconstruction task as an optimal transport problem involves constructing a cost matrix $M \in \mathbb{R}_+^{m \times n}$ representing distances between cells of X and spots of Y . Here, we used cosine distance $d_{cos}(X_{i,:}, Y_{j,:}) = 1 - \frac{\langle X_{i,:}, Y_{j,:} \rangle}{\|X_{i,:}\| \|Y_{j,:}\|}$, which is scale-invariant and can account for differences in measurement sensitivity between the two technologies. Furthermore, scale-invariant cosine dissimilarity is well-suited for handling the fact that expression of a spot in the spatial transcriptomics dataset is the mixture or sum of multiple cells in the scRNA-seq dataset. Specifically, the coupling matrix $\gamma \in \mathbb{R}_+^{m \times n}$ is solved for obtaining the optimal transport as follows:

$$\begin{aligned} \gamma^* \in \arg \min_{\gamma \in \mathbb{R}_+^{m \times n}} \sum_{i,j} \gamma_{i,j} M_{i,j} + \lambda \Omega(\gamma) \\ \text{s.t. } \gamma \mathbf{1} = m; \gamma^T \mathbf{1} = n; \gamma \geq 0 \end{aligned} \quad (2)$$

440 where $M \in \mathbb{R}_+^{m \times n}$ is the cost matrix defining the cost of moving gene expression from cell a_i to
 441 spot b_j and $\Omega(\gamma) = \sum_{i,j} \gamma_{i,j} \log(\gamma_{i,j})$ is an entropic regularization term [8]. The entropic regu-

442 larization version of optimal transport can be solved by Sinkhorn-Knopp’s alternative projection
443 algorithm [8]. In other words, this minimization process aims to match cells with similar expres-
444 sion profiles to spots with similar transcriptomic characteristics, measured by cosine similarity,
445 thereby capturing the underlying biological relationships between the two datasets.

446 It is important to note that we utilized the entropy regularization version of optimal trans-
447 port, resulting in a probabilistic mapping between cells and spots. This probabilistic coupling,
448 represented by the left-stochastic matrix γ , indicates the likelihood of a specific cell being as-
449 sociated with a particular spot. This probabilistic coupling offers computational efficiency and
450 eliminates assumptions about the number of cells in a spot, including cases where a cell may
451 reside on the boundary of two spots.

452 **4.4 Combination of deconvolution and mapping**

453 OT for spatial and scRNA-Seq data is challenging since spatial data is often sparse leading to
454 less dependable inferred individual cell-spot pairs. We thus further extend OT by incorporat-
455 ing the deconvolution result, which, as mentioned above, maps a group of cells to a group of
456 spots. As a result, scDOT integrates the two mentioned data modalities, single-cell and spatial
457 transcriptomics, by simultaneously solving the deconvolution and OT problems. Specifically,
458 given paired data modalities X and Y , representing gene expression profiles of a scRNA-seq
459 and a spatial transcriptomics data respectively, scDOT simultaneously solves the deconvolution
460 problem of estimating cell type fractions, P , of c cell types across m spots, and the spatial recon-
461 struction problem of mapping n cells to their m spatial origins, resulting in a coupling matrix
462 γ . These two solutions are constrained by the relation $\gamma \times C = P$, where C is a binary matrix
463 representing the cell type of each cell, encoded as a one-hot vector of size $1 \times c$ across the total n
464 cells. The two results, P and γ , are computed simultaneously in an iterative manner in order to
465 improve each other’s accuracy. The problem is then formed as a bi-level optimization where the
466 deconvolution and the spatial reconstruction are two inner optimization problems nested inside
467 the outer optimization that reflects the relation $\gamma \times C = P$. See Supporting Methods for more
468 details.

469 **4.5 Inference of cell-cell spatial neighborhood graph**

Utilizing the coupling matrix learned from optimal transport, we employed manifold alignment
[47, 36] to project the single-cell data X and spatial coordinates $Z \in \mathbb{R}^{m \times 2}$ of spatial transcrip-
tomics data onto a common nonlinear subspace. This subspace preserves the correspondence

between cells and spots, as well as the intrinsic similarity within each dataset. Consequently, in the common subspace, cells are represented in terms of both gene expression and spatial coordinates. Subsequently, we constructed a k-nearest neighbor graph (k-NNG) based on this new representation, which consists of the new coordinates in the common subspace for each cell. This allowed us to obtain the cell-cell spatial neighborhood graph. (In our experiments, we set $k = 10$.) The projections f and g resulting from manifold alignment serve as minimizers of the following optimization problem, which can be formulated as a generalized eigenvalue problem:

$$\begin{aligned} f^*, g^* = \arg \min_{f, g} & (1 - \mu) \sum_{i=1}^m \sum_{j=1}^n \|f(x_i) - g(z_j)\|_2^2 \gamma^{i,j} \\ & + \mu \sum_{i=1}^m \sum_{j=1}^n \|f(x_i) - f(x_j)\|_2^2 W_X^{i,j} \\ & + \mu \sum_{i=1}^m \sum_{j=1}^n \|g(x_i) - g(z_j)\|_2^2 W_Z^{i,j} \end{aligned} \quad (3)$$

470 where W_X and W_Z are adjacent matrices of kNN graphs of X and Z , respectively.

471 References

- 472 [1] Diana Álvarez, Nayra Cárdenes, Jacobo Sellarés, Marta Bueno, Catherine Corey,
473 Vidya Sagar Hanumanthu, Yating Peng, Hannah D’Cunha, John Sembrat, Mehdi Nouraié,
474 et al. Ipf lung fibroblasts have a senescent phenotype. *American Journal of Physiology-Lung
475 Cellular and Molecular Physiology*, 313(6):L1164–L1173, 2017.
- 476 [2] Alma Andersson, Joseph Bergenstråhle, Michaela Asp, Ludvig Bergenstråhle, Aleksandra
477 Jurek, José Fernández Navarro, and Joakim Lundeberg. Single-cell and spatial transcrip-
478 tomics enables probabilistic inference of cell type topography. *Communications biology*,
479 3(1):565, 2020.
- 480 [3] Tommaso Biancalani, Gabriele Scalia, Lorenzo Buffoni, Raghav Avasthi, Ziqing Lu, Aman
481 Sanger, Neriman Tokcan, Charles R Vanderburg, Åsa Segerstolpe, Meng Zhang, et al. Deep
482 learning and alignment of spatially resolved single-cell transcriptomes with tangram. *Nature
483 methods*, 18(11):1352–1362, 2021.
- 484 [4] Andrew Butler, Paul Hoffman, Peter Smibert, Efthymia Papalexi, and Rahul Satija. Inte-
485 grating single-cell transcriptomic data across different conditions, technologies, and species.
486 *Nature biotechnology*, 36(5):411–420, 2018.

- 487 [5] Dylan M Cable, Evan Murray, Luli S Zou, Aleksandrina Goeva, Evan Z Macosko, Fei Chen,
488 and Rafael A Irizarry. Robust decomposition of cell type mixtures in spatial transcriptomics.
489 *Nature Biotechnology*, 40(4):517–526, 2022.
- 490 [6] Yanshuo Chen, Yixuan Wang, Yuelong Chen, Yuqi Cheng, Yumeng Wei, Yunxiang Li, Jium-
491 ing Wang, Yingying Wei, Ting-Fung Chan, and Yu Li. Deep autoencoder for interpretable
492 tissue-adaptive deconvolution and cell-type-specific gene analysis. *Nature Communications*,
493 13(1):6735, 2022.
- 494 [7] Benoît Colson, Patrice Marcotte, and Gilles Savard. An overview of bilevel optimization.
495 *Annals of operations research*, 153:235–256, 2007.
- 496 [8] Marco Cuturi. Sinkhorn distances: Lightspeed computation of optimal transport. *Advances*
497 *in neural information processing systems*, 26, 2013.
- 498 [9] Marie Deprez, Laure-Emmanuelle Zaragosi, Marin Truchi, Christophe Becavin, Sandra
499 Ruiz García, Marie-Jeanne Arguel, Magali Plaisant, Virginie Magnone, Kevin Lebrigand,
500 Sophie Abelanet, et al. A single-cell atlas of the human healthy airways. *American journal*
501 *of respiratory and critical care medicine*, 202(12):1636–1645, 2020.
- 502 [10] Rui Dong and Guo-Cheng Yuan. Spatialdws: accurate deconvolution of spatial transcrip-
503 tomic data. *Genome biology*, 22(1):145, 2021.
- 504 [11] Mirjana Efremova, Miquel Vento-Tormo, Sarah A Teichmann, and Roser Vento-Tormo.
505 Cellphonedb: inferring cell–cell communication from combined expression of multi-subunit
506 ligand–receptor complexes. *Nature protocols*, 15(4):1484–1506, 2020.
- 507 [12] Marc Elosua-Bayes, Paula Nieto, Elisabetta Mereu, Ivo Gut, and Holger Heyn. Spotlight:
508 seeded nmf regression to deconvolute spatial transcriptomics spots with single-cell tran-
509 scriptomes. *Nucleic acids research*, 49(9):e50–e50, 2021.
- 510 [13] Juan Antonio Fafián-Labora and Ana O’Loghlen. Classical and nonclassical intercellular
511 communication in senescence and ageing. *Trends in Cell Biology*, 30(8):628–639, 2020.
- 512 [14] Xu Feng, Liwen Wang, Ruoyu Zhou, Rui Zhou, Linyun Chen, Hui Peng, Yan Huang,
513 Qi Guo, Xianghang Luo, and Haiyan Zhou. Senescent immune cells accumulation promotes
514 brown adipose tissue dysfunction during aging. *Nature Communications*, 14(1):3208, 2023.
- 515 [15] Nathan S Gasek, George A Kuchel, James L Kirkland, and Ming Xu. Strategies for targeting
516 senescent cells in human disease. *Nature aging*, 1(10):870–879, 2021.
- 517 [16] Stephen Gould, Richard Hartley, and Dylan Campbell. Deep declarative networks. *IEEE*
518 *Transactions on Pattern Analysis and Machine Intelligence*, 44(8):3988–4004, 2021.

- 519 [17] Katharina Heinzlmann, Qianjiang Hu, Yan Hu, Evgenia Dobrinskikh, Meshal Ansari,
520 M Camila Melo-Narváez, Henrik M Ulke, Colton Leavitt, Carol Mirita, Tammy Trudeau,
521 et al. Single-cell rna sequencing identifies g-protein coupled receptor 87 as a basal cell
522 marker expressed in distal honeycomb cysts in idiopathic pulmonary fibrosis. *European*
523 *Respiratory Journal*, 59(6), 2022.
- 524 [18] Richard J Hewitt and Clare M Lloyd. Regulation of immune responses by the airway
525 epithelial cell landscape. *Nature Reviews Immunology*, 21(6):347–362, 2021.
- 526 [19] Nikos Karaiskos, Philipp Wahle, Jonathan Alles, Anastasiya Boltengagen, Salah Ayoub,
527 Claudia Kipar, Christine Kocks, Nikolaus Rajewsky, and Robert P Zinzen. The drosophila
528 embryo at single-cell transcriptome resolution. *Science*, 358(6360):194–199, 2017.
- 529 [20] Namjin Kim and Thiennu H Vu. Parabronchial smooth muscle cells and alveolar myofi-
530 broblasts in lung development. *Birth Defects Research Part C: Embryo Today: Reviews*,
531 78(1):80–89, 2006.
- 532 [21] Vitalii Kleshchevnikov, Artem Shmatko, Emma Dann, Alexander Aivazidis, Hamish W
533 King, Tong Li, Rasa Elmentaite, Artem Lomakin, Veronika Kedlian, Adam Gayoso, et al.
534 Cell2location maps fine-grained cell types in spatial transcriptomics. *Nature biotechnology*,
535 40(5):661–671, 2022.
- 536 [22] Charles L Lawson and RJ Hanson. Linear least squares with linear inequality constraints.
537 *Solving least squares problems*, pages 158–173, 1974.
- 538 [23] Bin Li, Wen Zhang, Chuang Guo, Hao Xu, Longfei Li, Minghao Fang, Yinlei Hu, Xinye
539 Zhang, Xinfeng Yao, Meifang Tang, et al. Benchmarking spatial and single-cell transcrip-
540 tomics integration methods for transcript distribution prediction and cell type deconvolu-
541 tion. *Nature methods*, 19(6):662–670, 2022.
- 542 [24] Haoyang Li, Juexiao Zhou, Zhongxiao Li, Siyuan Chen, Xingyu Liao, Bin Zhang, Ruochi
543 Zhang, Yu Wang, Shiwei Sun, and Xin Gao. A comprehensive benchmarking with practical
544 guidelines for cellular deconvolution of spatial transcriptomics. *Nature Communications*,
545 14(1):1548, 2023.
- 546 [25] Chih-Jen Lin. Projected gradient methods for nonnegative matrix factorization. *Neural*
547 *computation*, 19(10):2756–2779, 2007.
- 548 [26] Yifan Lin and Zhihao Xu. Fibroblast senescence in idiopathic pulmonary fibrosis. *Frontiers*
549 *in Cell and Developmental Biology*, 8:593283, 2020.
- 550 [27] Alexandra F Long and Tim Stearns. A not-so-simple twist of fate. *Developmental Cell*,
551 56(4):402–404, 2021.

- 552 [28] Sophia K Longo, Margaret G Guo, Andrew L Ji, and Paul A Khavari. Integrating single-
553 cell and spatial transcriptomics to elucidate intercellular tissue dynamics. *Nature Reviews*
554 *Genetics*, 22(10):627–644, 2021.
- 555 [29] Romain Lopez, Baoguo Li, Hadas Keren-Shaul, Pierre Boyeau, Merav Kedmi, David Pilzer,
556 Adam Jelinski, Ido Yofe, Eyal David, Allon Wagner, et al. Destvi identifies continuums of
557 cell types in spatial transcriptomics data. *Nature biotechnology*, 40(9):1360–1369, 2022.
- 558 [30] Ying Ma and Xiang Zhou. Spatially informed cell-type deconvolution for spatial transcrip-
559 tomics. *Nature biotechnology*, 40(9):1349–1359, 2022.
- 560 [31] Mozhdeh Mehdizadeh, Martin Aguilar, Eric Thorin, Gerardo Ferbeyre, and Stanley Nattel.
561 The role of cellular senescence in cardiac disease: basic biology and clinical relevance. *Nature*
562 *Reviews Cardiology*, 19(4):250–264, 2022.
- 563 [32] Brendan F Miller, Feiyang Huang, Lyla Atta, Arpan Sahoo, and Jean Fan. Reference-free
564 cell type deconvolution of multi-cellular pixel-resolution spatially resolved transcriptomics
565 data. *Nature communications*, 13(1):2339, 2022.
- 566 [33] Jeffrey R Moffitt, Dhananjay Bambah-Mukku, Stephen W Eichhorn, Eric Vaughn, Karthik
567 Shekhar, Julio D Perez, Nimrod D Rubinstein, Junjie Hao, Aviv Regev, Catherine Dulac,
568 et al. Molecular, spatial, and functional single-cell profiling of the hypothalamic preoptic
569 region. *Science*, 362(6416):eaau5324, 2018.
- 570 [34] Karthik Nagaraj, Rive Sarfstein, Zvi Laron, and Haim Werner. Long-term igf1 stimula-
571 tion leads to cellular senescence via functional interaction with the thioredoxin-interacting
572 protein, txnip. *Cells*, 11(20):3260, 2022.
- 573 [35] Yuki Nakamura, Hisataka Iwata, Takehito Kuwayama, and Koumei Shirasuna. S100a8,
574 which increases with age, induces cellular senescence-like changes in bovine oviduct epithelial
575 cells. *American Journal of Reproductive Immunology*, 82(3):e13163, 2019.
- 576 [36] Nam D Nguyen and Daifeng Wang. Multiview learning for understanding functional mul-
577 tiomics. *PLoS computational biology*, 16(4):e1007677, 2020.
- 578 [37] Mor Nitzan, Nikos Karaiskos, Nir Friedman, and Nikolaus Rajewsky. Gene expression
579 cartography. *Nature*, 576(7785):132–137, 2019.
- 580 [38] Michael Overholtzer. Senescent cells feed on their neighbours, 2019.
- 581 [39] Branca I Pereira, Oliver P Devine, Milica Vukmanovic-Stejic, Emma S Chambers, Priya
582 Subramanian, Neil Patel, Alex Virasami, Neil J Sebire, Veronica Kinsler, Alexis Valdovi-

- 583 nos, et al. Senescent cells evade immune clearance via hla-e-mediated nk and cd8+ t cell
584 inhibition. *Nature communications*, 10(1):2387, 2019.
- 585 [40] Gabriel Peyré, Marco Cuturi, et al. Computational optimal transport. *Center for Research*
586 *in Economics and Statistics Working Papers*, (2017-86), 2017.
- 587 [41] Rebecca Peyser, Scott MacDonnell, Yinglin Gao, Luis Cheng, Yong Kim, Theodore Ka-
588 plan, Qin Ruan, Yi Wei, Min Ni, Christina Adler, et al. Defining the activated fibroblast
589 population in lung fibrosis using single-cell sequencing. *American journal of respiratory cell*
590 *and molecular biology*, 61(1):74–85, 2019.
- 591 [42] Valeria Severino, N Alessio, Annarita Farina, A Sandomenico, M Cipollaro, G Peluso,
592 U Galderisi, and A Chambery. Insulin-like growth factor binding proteins 4 and 7 released
593 by senescent cells promote premature senescence in mesenchymal stem cells. *Cell death &*
594 *disease*, 4(11):e911–e911, 2013.
- 595 [43] Tim Stuart, Andrew Butler, Paul Hoffman, Christoph Hafemeister, Efthymia Papalexi,
596 William M Mauck, Yuhan Hao, Marlon Stoeckius, Peter Smibert, and Rahul Satija. Com-
597 prehensive integration of single-cell data. *Cell*, 177(7):1888–1902, 2019.
- 598 [44] Eleanor Valenzi, Melissa Bulik, Tracy Tabib, Christina Morse, John Sembrat, Hum-
599 berto Trejo Bittar, Mauricio Rojas, and Robert Lafyatis. Single-cell analysis reveals fi-
600 broblast heterogeneity and myofibroblasts in systemic sclerosis-associated interstitial lung
601 disease. *Annals of the rheumatic diseases*, 78(10):1379–1387, 2019.
- 602 [45] Cédric Villani et al. *Optimal transport: old and new*, volume 338. Springer, 2009.
- 603 [46] Benjamin L Walker, Zixuan Cang, Honglei Ren, Eric Bourgain-Chang, and Qing Nie. De-
604 ciphering tissue structure and function using spatial transcriptomics. *Communications bi-*
605 *ology*, 5(1):220, 2022.
- 606 [47] Chang Wang and Sridhar Mahadevan. A general framework for manifold alignment. In
607 *2009 AAAI Fall Symposium Series*, 2009.
- 608 [48] David W Waters, Kaj EC Blokland, Prabuddha S Pathinayake, Janette K Burgess, Steven E
609 Mutsaers, Cecilia M Prele, Michael Schuliga, Christopher L Grainge, and Darryl A Knight.
610 Fibroblast senescence in the pathology of idiopathic pulmonary fibrosis. *American Journal*
611 *of Physiology-Lung Cellular and Molecular Physiology*, 315(2):L162–L172, 2018.
- 612 [49] Joshua D Welch, Velina Kozareva, Ashley Ferreira, Charles Vanderburg, Carly Martin, and
613 Evan Z Macosko. Single-cell multi-omic integration compares and contrasts features of brain
614 cell identity. *Cell*, 177(7):1873–1887, 2019.

- 615 [50] Lulu Yan and Xiaoqiang Sun. Benchmarking and integration of methods for deconvoluting
616 spatial transcriptomic data. *Bioinformatics*, 39(1):btac805, 2023.
- 617 [51] Yingkun Zhang, Xinrui Lin, Zhixian Yao, Di Sun, Xin Lin, Xiaoyu Wang, Chaoyong Yang,
618 and Jia Song. Deconvolution algorithms for inference of the cell-type composition of the
619 spatial transcriptome. *Computational and Structural Biotechnology Journal*, 2022.